

Article

In Vitro Degradation Behavior, Mechanical Properties, and Cytocompatibility of Biodegradable Mg-1Zn-xSn Alloys

Weiyan Jiang¹ and Wenzhou Yu^{2,*} 

¹ Engineering Research Centre for Waster Oil Recovery Technology and Equipment, Ministry of Education, Chongqing Technology and Business University, Chongqing 400067, China

² College of Materials Science and Engineering, Chongqing University, Chongqing 400045, China

* Correspondence: yuwenzhoucd@cqu.edu.cn; Tel.: +86-23-65112631

Abstract: The application of biodegradable alloys in orthopedic implants has gained widespread attention globally. Magnesium alloys with controllable degradation rate and suitable mechanical properties have been regarded as potential orthopedic implant material. In this paper, a Mg-1Zn-xSn (x = 0, 1.0, 1.5, 2.0 wt.%) ternary alloy was designed and its performance was investigated. Compared with the Mg-1Zn alloy, the Mg-1Zn-xSn alloys showed enhanced mechanical properties and in vitro degradation performance. Above all, the extruded Mg-1Zn-1.0Sn alloy exhibited an extremely low corrosion rate of 0.12 mm/y with a low hydrogen release of 0.021 mL/cm²/day, which can be attributed to the hydrogen release suppression effect caused by Sn and SnO₂ formation in the surface of the alloy. The cytotoxicity of the Mg-1Zn-1.0Sn alloy was evaluated by the cell counting kit-8 (CCK-8) method, the results of which show that its cytotoxicity grade is zero, and the MC3T3-E1 cells spread well on the alloy surface. The findings in this paper demonstrated that Mg-1Zn-1.0Sn is a potential candidate for biodegradable material in the orthopedic implant field.

Keywords: magnesium alloys; mechanical properties; degradation; cytocompatibility



Citation: Jiang, W.; Yu, W. In Vitro Degradation Behavior, Mechanical Properties, and Cytocompatibility of Biodegradable Mg-1Zn-xSn Alloys. *Crystals* **2022**, *12*, 1219. <https://doi.org/10.3390/cryst12091219>

Academic Editor: Cyril Cayron

Received: 11 August 2022

Accepted: 26 August 2022

Published: 29 August 2022

Publisher's Note: MDPI stays neutral with regard to jurisdictional claims in published maps and institutional affiliations.



Copyright: © 2022 by the authors. Licensee MDPI, Basel, Switzerland. This article is an open access article distributed under the terms and conditions of the Creative Commons Attribution (CC BY) license (<https://creativecommons.org/licenses/by/4.0/>).

1. Introduction

Magnesium (Mg) alloy is a promising degradation material in the orthopedic implant field. One of its key advantages is the mechanical compatibility with natural bone. For instance, its low elastic modulus ($E = 41\text{--}45$ GPa) and density ($1.74\text{--}1.84\text{g/cm}^3$) are a good approximation to those of natural bone ($E = 3\text{--}20$ GPa and density = $1.8\text{--}2.1$ g/cm³), which will effectively avoid the stress shielding effects [1]. Furthermore, Mg ions are common metabolites in the human body, with a daily consumption of 250–300 mg/day, and naturally stored in bones [2]. The biocompatibility and the moderate mechanical properties make Mg alloys outstanding as materials for orthopedic implants. Unfortunately, the main disadvantage of Mg alloys as the degradation material is their rapid degradation during service.

In order to overcome this disadvantage, various techniques, including surface modification, structure optimization, and composition design, have been developed to control the biological degradation rate [1–3]. Surface modification is the most direct way to improve the surface coating and degradation rate of Mg alloys; however, coating damage often causes rapid corrosion followed by unpredictable mechanical collapse and high local concentration of released metallic ions [4,5]. Regarding the optimization of the structure, amorphous and porous structure have been attempted to regulate the Mg degradation. However, their other performance characteristics should be further improved. For example, porous structure is beneficial for decreasing the degradable rate, but the mechanical properties are weakened compared to the bulk materials [6,7]. Up to now, the composition design of Mg alloys has been attracting the majority of researchers because it can integrate almost all the benefits above. The recently developed Mg-Li-based alloy exhibited

satisfying mechanical properties and a low degradation rate. The reduced corrosion rate is attributed to the rapid formation of a stable self-healing protective carbonate-rich film (Li_2CO_3) and an underlying compact $\text{Li}_2\text{O}/\text{MgO}$ layer on the Mg matrix, which seems like a natural self-repairing surface modification process [8]. Hence, the selection of alloying elements is critical. Currently, pure Mg, Mg-Al [9–11], Mg-RE [12–14], and Al- and/or RE-free alloys [15–17] are the four major groups of biodegradable Mg alloys. Al- and RE-containing alloys usually present high strength and high corrosion resistance. However, the released metallic ions affect the cells of the surrounding tissue. Some *in vivo* studies [3] showed that AZ91D and LAE442 alloys presented the risk of causing nerve toxicity, and RE elements were controversial for being easily deposited in the brain. Therefore, biologically safe elements with low content are desirable for inclusion among biomedical Mg alloys for clinical use.

Zinc (Zn) is a frequently used alloying element in Mg alloys. The addition of Zn could reduce the corrosion rate and improve the mechanical strength because it can form solid solution and change the performance of Mg alloys [18]. During the thermal treatment, it has the ability to transform impurities such as Iron (Fe), Silicon (Si), and Nickel (Ni) into harmless intermetallics, thereby reducing the corrosion rate [19,20]. Additionally, as a nutrient essential to the human body, low content of Zn [21] was proved to be biologically safe. Mg-1Zn alloy with a microstructure of single solid solution presented a good biocompatibility and less hydrogen gas release than many other binary Mg alloys in simulated body fluid [22,23]. However, the mechanical properties and degradation rate should be further regulated for practical clinical application [24,25]. Tin (Sn) is also an essential trace element in the human body with a high solid solubility in Mg alloys at eutectic temperature. Solid solution Sn will improve the electrode potential of Mg matrix to improve the corrosion resistance. According to previous reports for Mg-1Sn alloy, it exhibited a good *in vitro* biocompatibility [21]. Moreover, the addition of Sn to Mg alloys improved their strength and creep properties at elevated temperatures, due to the solid solution strengthening and the high melting point of Mg_2Sn phase [26]. The corrosion rate of Mg-xSn alloys was significantly decreased by increasing the volume ratio of solid solution Sn, while the increased Mg_2Sn phase accelerated the corrosion process [27]. However, the effect of low content Sn on the *in vitro* degradation behavior of Mg-1Zn alloys is still not fully understood. In order to obtain an optimal Mg alloy with low content of alloying elements for orthopedic implants, Sn was selected to design Mg-1Zn-xSn ($x = 0, 1.0, 1.5, 2.0$ wt.%) ternary alloys in the current work. The microstructure, mechanical properties, degradation behavior, and *in vitro* cytocompatibility were systematically investigated, and the influence mechanism of Sn on the degradation rate was preliminarily clarified.

2. Materials and Methods

2.1. Materials Preparation

High purified Mg (99.98 wt.%), Zn (99.99 wt.%), and Sn (99.99 wt.%) with a proper ratio were melted in an induction furnace under Ar gas protection. The prepared Mg-1Zn-xSn ($x = 0, 1.0, 1.5, \text{ and } 2.0$ wt.%) alloy ingots 80 mm in diameter were then extruded into a bar with a ratio of 25, at a temperature of 300 °C. The samples cut from the extruded bars were successively ground to 1400 grit by SiC paper, ultrasonically cleaned in deionized water and ethanol, and dried in cold air. For reproducibility, three replicates were prepared for each test.

2.2. Microstructure Characterization

The samples were polished first, and then etched by a mixed solution with saturated picric acid, 2 mL acetic acid, and 8 mL ethanol for microstructure observation [25]. The microstructure of the samples was measured by X-ray diffraction (XRD, Rigaku D/MAX-2500PC, Tokyo, Japan) with Cu $K\alpha$ radiation, and scanning electron microscopy (SEM, VegaIII MU, Brno, Czech Republic), equipped with an energy dispersive X-ray spectrometer (EDS, Oxford Instrument INKAX-sight; Oxford Instrument, Oxford, UK).

2.3. Mechanical Properties

According to ASTM E8/E8M-13a, the as-extruded bars with a diameter of 16 mm were processed into tensile samples 2 mm in gauge thickness, 5 mm in gauge width, and 10 mm in gauge length. The compression samples were prepared, according to ASTM E9-19, with a diameter of 5 mm and a height of 10 mm, respectively. The tension and compression tests were conducted on a SANS CMT5105 testing machine at room temperature with a strain rate of 10^{-3} s^{-1} and $1 \text{ mm} \cdot \text{min}^{-1}$, respectively.

2.4. Degradation Properties

2.4.1. In Vitro Degradation by Electrochemical Measurements

Electrochemical measurements to evaluate the in vitro degradation behavior were carried out at $37 \text{ }^\circ\text{C}$ in phosphate buffer solution (PBS). The samples were embedded in self-curing denture acrylic, and the exposed area was 0.785 cm^2 (10 mm in diameter). These samples were used as working electrodes in a three-electrode system, in which a platinum plate was used as counter electrode, and a saturated calomel electrode (SCE) was used as reference electrode. In order to get a relatively stable state of the system, 30 min of the open-circuit potential was measured at first before the electrochemical measurements. The potentiodynamic polarization curve was fitted by CView software (Wuhan CorrTest Co. Ltd., Wuhan, China). Meanwhile, the Nyquist plot of the electrochemical impedance spectroscopy (EIS) test was fitted by ZView software (Wuhan CorrTest Co. Ltd., Wuhan, China) [28].

2.4.2. In Vitro Degradation by Immersion Tests

The immersion tests were conducted in PBS at $37 \text{ }^\circ\text{C}$ according to ASTM-G31-72 by hydrogen release collection and mass loss method [29]. The samples with the size of $10 \times 10 \times 7 \text{ mm}$ were immersed in PBS solution according to a ratio of 20 mL/cm^2 . In this test, the pH value of the solution was measured by a pH meter (PHS-3C pH Meter). Hydrogen was collected in an inverted funnel and recorded by a scaled burette. After 7 days, corrosion products formed on samples were cleaned in a mixed solution containing 200 g/L of chromic acid and 10 g/L of AgNO_3 . The surface morphologies were examined by SEM. XRD was employed to determine the phase composition of corrosion products. The average corrosion rate CR (mm/y) can be calculated by the following Equation (1):

$$\text{CR} = (\text{K} \times \text{W}) / (\text{A} \times \text{T} \times \text{D}) \quad (1)$$

In which K is a constant 8.76×10^4 , W is the mass loss (g), A is the exposed surface area in solution (cm^2), T is the time of immersion test (h), and D is the density of the sample (g/cm^3).

2.5. Cytocompatibility

Dulbecco's modified Eagle's medium/F12 (DMEM/F12; Hyclone, Logan, UT, USA) with 10% fetal bovine serum and MC3T3-E1 cells at passage 3–4 were used for cell culture.

2.5.1. Cytotoxicity Assays and Cell Spreading

DMEM/F12 containing 10% FBS was used as the extraction medium, with a surface area/extraction medium ratio of $1.25 \text{ cm}^2/\text{mL}$. In this experiment, the extract solution of pure Mg (as control) and Mg-1Zn-1.0Sn was serially diluted to 10%, 30%, 50%, and 100% concentration in a humidified atmosphere with 5% CO_2 at $37 \text{ }^\circ\text{C}$ (DMEM/F12 as a negative control). A cell counting kit-8 (CCK-8; Beyotime) was used to evaluate cell viability. A $200 \text{ }\mu\text{L}$ cell suspension was seeded in a 96-well plate with a cell density of 2×10^4 viable cells/mL per well. After 72 h, $20 \text{ }\mu\text{L}$ CCK-8 solution was added to each well, and then the plate was incubated for 4 h. The spectrophotometrical absorbance of the plates were

measured at 450 nm using a microplate reader (Thermo Fisher Scientific, Waltham, MA, USA). The relative growth rate (RGR) was calculated according to Equation (2):

$$\text{RGR} = \frac{\text{OD}_{\text{test}}}{\text{OD}_{\text{control}}} \times 100\% \quad (2)$$

Cell spreading was evaluated by observing the cell microfilaments of the MC3T3-E1 cells. After co-culturing with the extraction of Mg-1Zn-1.0Sn alloy for 24 h, the cells were washed three times with PBS, and fixed with 3.7% paraformaldehyde for 15 min at room temperature. Then, 0.1% Triton X-100 was used to permeabilize the cells for 5 min. After being washed with PBS again, the cells were stained with rhodamine-phalloidin (50 µg/mL; Sigma-Aldrich, Shanghai, China) at room temperature for 30 min. Then, after being washed three times, the cells were stained with 4, 6-diamidino-2-phenylindole (0.1 µg/mL; Sigma-Aldrich, Shanghai, China) for 15 min. Finally, the cell microfilament cytoskeleton and nucleus were observed (cells cultured in DMEM/F12 as a control) by CLSM using a LSM800 confocal Laser microscopy (Carl Zeiss, Oberkochen, Baden-Württemberg, German).

2.5.2. Cell Attachment

The Mg-1Zn-1.0Sn alloy and pure Mg (as control) were co-cultured with cells in a 24 plate. The cell density of each well was 2×10^4 viable cells per cm^2 . After co-culturing for 24 h, the cells on the samples were carefully washed with PBS three times and fixed with 2.5% glutaraldehyde for 15 min. After that, the cells were dehydrated in a series of ethanol concentrations from low to high (30%, 50%, 70%, 90%, and 100% for 15 min each time). Finally, all the samples were dried, sputter-coated with gold, and observed by SEM.

3. Results and Discussion

3.1. Microstructure Analysis

Figure 1 presents the SEM-backscattered electron photos of the extruded Mg-1Zn-xSn alloys. It can be seen that the alloys exhibited α -Mg solid solution with small dispersed white particles of different quantities. The unequal-sized grains vary from about 5 µm to 30 µm in the Mg-1Zn alloy, and the average grain size determined by image analysis (Image-Pro plus 6.0 software, Media Cybernetics, Maryland, USA) is approximately 25 µm. A very few tiny white particles with sizes from 0.6–1 µm are characterized by EDS (as seen in Table 1), which demonstrates particle I in Figure 1a is composed of Mg, O, Si and Fe, implying that Zn was totally dissolved into the Mg matrix as solid solution.

As for Sn-containing alloys, the grain boundaries are difficult to expose, and some grains of about 4–10 µm are confirmed in the Mg-1Zn-1.0Sn alloy. As widely reported, the grain size of Mg alloys would decrease with increasing Sn, due to the refinement effect of the Sn element [30–32]. For example, the average grain sizes of Mg-4Zn-1.5Al-xSn ($x = 0, 0.5, 1.0, 2.0, 3.0$) alloys are 9.9 µm, 7.7 µm, 6.2 µm, 4.7 µm, and 5.5 µm, respectively [32]. Therefore, it is concluded that the grain size might decrease by increasing Sn content. In addition, the small white particles exhibit a tendency to grow bigger and multiply, compared with Mg-1Zn alloy. It is certain that there is no Sn-containing ternary phase formed in the Mg-Zn-Sn alloy system [33]. The formation of the intermetallics is related to the electronegative difference between different elements [34]. Therefore, Mg_2Sn phase is preferred to form in the Mg-Zn-Sn alloy because of the highest electronegative difference between Mg and Sn elements. However, the white particles II, III, and IV shown in Figure 1b–d are mainly composed of Mg, O, Sn, Si, and Fe, indicating that Mg_2Sn phases always combine with impurities such as Fe and Si, to purify the Mg matrix. Figure 2 shows the XRD result of the investigated alloys. It can be observed that the Mg-1Zn alloy is composed of α -Mg and dispersed impurities, while Sn-containing alloys consist of α -Mg and dispersed Mg_2Sn phase, combining with some impurities. With increases in added Sn, the intensity of diffraction peaks is enhanced, especially for Mg_2Sn . This implies that the amount of Mg_2Sn phase increases with the increasing addition of Sn, and the peaks

of Mg_2Sn phase can only be found in Mg-1Zn-1.5Sn and Mg-1Zn-2.0Sn alloy within the detection limit of XRD.

Table 1. Chemical compositions of the white particles in Mg-1Zn-based alloys (wt.%).

Alloy	Points	Element (wt.%)					Total
		Mg	O	Sn	Si	Fe	
Mg-1Zn	I	11.97	3.96		2.77	81.30	100
Mg-1Zn-1.0Sn	II	71.54	15.56	4.34	2.17	6.39	100
Mg-1Zn-1.5Sn	III	56.10	22.94	9.78	1.25	7.14	100
Mg-1Zn-2.0Sn	IV	49.49	25.65	21.79	3.07	-	100

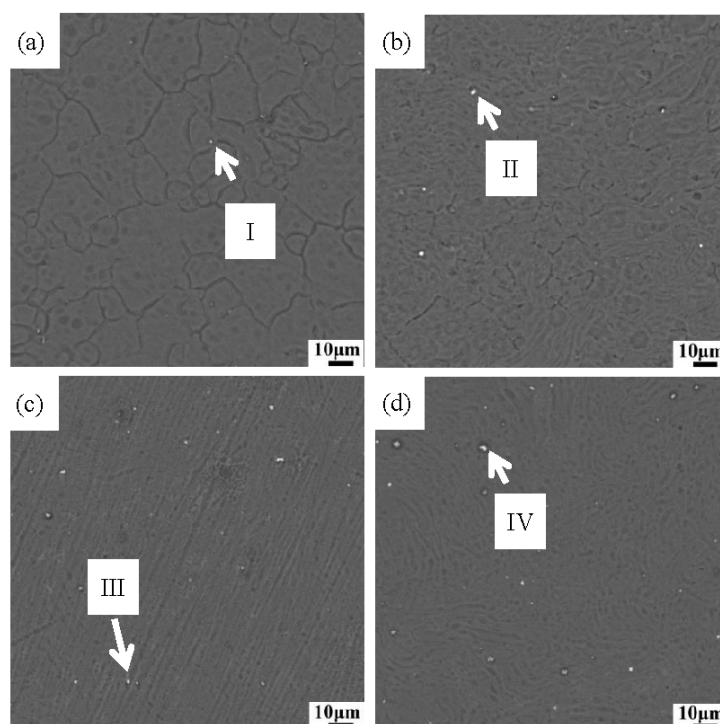


Figure 1. Microstructures of Mg-1Zn-based alloys: Mg-1Zn (a), Mg-1Zn-1.0Sn (b), Mg-1Zn-1.5Sn (c), and Mg-1Zn-2.0Sn (d).

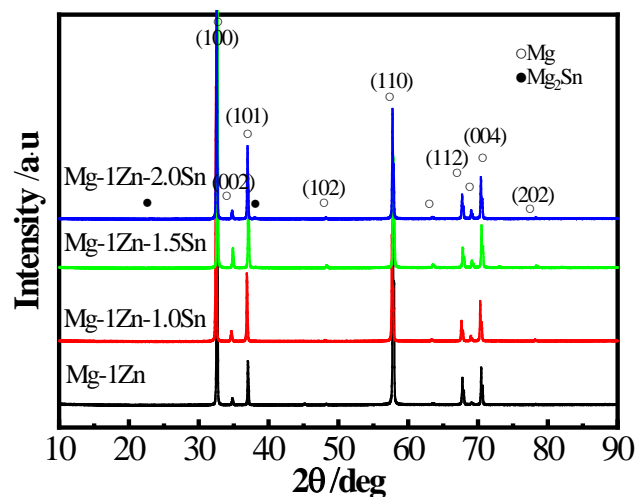


Figure 2. XRD patterns of Mg-1Zn-xSn ternary alloys.

3.2. Mechanical Properties

The tensile stress–strain curves (Figure 3a) and compression stress–strain curves (Figure 3b) demonstrated that the current alloys have a good mechanical property. It is shown in Table 2 that the yield strength (YS) and ultimate tensile strength (UTS) of all the specimens are higher than 100 MPa and 200 MPa, respectively. Clearly, the addition of 1.0Sn results in an increase of the strength and elongation. When the content of Sn increases to 1.5, the strength begins to decrease slightly. This phenomenon might be associated with the phase composition and distribution. The phase composition characterized by XRD shows that Mg₂Sn phase is the only second phase determined. The crystal lattice constants of the specimens calculated by Jade 6.5 are displayed in Table 3, which shows that the values of a, b, and c of these four alloys all deviated from that of pure Mg (PDF 35-0821) to some extent. The lattice constant deviation means the lattice distortion. The greater the parameters' deviation from Pure Mg, the greater the lattice distortion. Table 3 shows that the lattice parameters' deviation increases with the incremental addition of Sn content, which means that the lattice distortion increases actually contribute to the enhancement of strength. However, as the Sn content reached 1.5, the average grain size increased (Figure 1), which resulted in the weakening of the grain strengthening effect and a decrease in the mechanical properties. In spite of this, the present alloys show similar mechanical properties with natural bone [35] and the extruded AZ31 alloys [36], as shown in Table 2. AZ31 alloys have been investigated widely for orthopedic applications because of the good mechanical and corrosion properties. It is obvious that the Mg-Zn-Sn alloys have a similar strength and simultaneously have a higher elongation compared to the commercial AZ31 alloy. Additionally, it can be seen from Table 2 that the yield strength (YS) and ultimate tensile strength (UTS) of 1.0Sn alloy are improved compared with the Mg-1Zn alloy, which is attributed to the solid solution strengthening and dispersed Mg₂Sn precipitates. Since Mg-1Zn-1.0Sn and Mg-1Zn-1.5Sn alloys present good tensile performance, the compression tests were also performed, with results listed in Table 2. The results demonstrate the weak tension–compression yield asymmetry of these two alloys, implying that it can withstand different load modes such as tension and compression during their practical work.

Table 2. The mechanical properties of Mg-Zn-Sn alloys, bone, and AZ31 extruded alloys.

Alloys	Tensile Properties			Ref	Compression Properties		
	TYS (MPa)	UTS (MPa)	ϵ (%)		CYS (MPa)	UCS (MPa)	E (%)
Cortical bone	35–283	1.07–2.10	[34]		164–240		
AZ31 extruded	185	264	10.5	[35]			
Mg-1Zn	100 ± 3	229 ± 10	17.4 ± 1.2	Present	—	—	—
Mg-1Zn-1.0Sn	118 ± 5	259 ± 14	20.2 ± 1.8	Present	96 ± 5	376 ± 16	16.7 ± 1.4
Mg-1Zn-1.5Sn	115 ± 4	249 ± 11	27.0 ± 2.1	Present	95 ± 4	367 ± 17	31.4 ± 1.6
Mg-1Zn-2.0Sn	112 ± 6	245 ± 12	23.1 ± 1.9	Present	—	—	—

Table 3. Lattice constants of the specimens calculated from XRD patterns.

Specimens	a (Å)	b (Å)	c (Å)	D (nm)
Mg (PDF35-0821)	3.21	3.21	5.21	—
Mg-1Zn	3.17	3.17	4.78	79.6
Mg-1Zn-1.0Sn	3.19	3.19	4.99	61.7
Mg-1Zn-1.5Sn	4.10	4.10	5.32	65.1
Mg-1Zn-2.0Sn	4.20	4.20	5.37	69.5

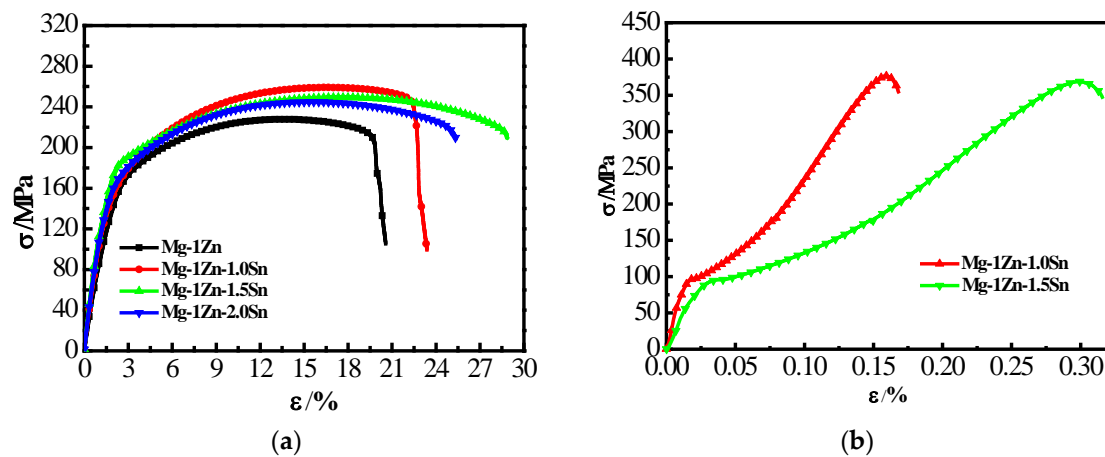


Figure 3. Mechanical properties of Mg-1Zn-xSn ternary alloys: tensile curves (a), compressive curves (b).

3.3. In Vitro Degradation Properties

The potentiodynamic polarization curves of the studied alloys are shown in Figure 4a. Compared to the Sn-free alloy, the Sn-containing alloys display higher cathodic current density but lower anodic current density. After Sn addition, the increased number of second phases leads to the increase of cathodic hydrogen evolution sites, resulting in higher cathodic current density of the Sn-containing alloys. For the high hydrogen evolution, the overvoltage of Sn can suppress hydrogen release to some extent [36], and the cathodic currents of all the alloys are approximately at the same level. Considering the anodic branch, the alloys present a passivation tendency below the breakdown potential (E_b), which indicates protective films formation above the surfaces of the samples. The related electrochemical parameters are shown in Table 4. From these data, it is clear that the effect of Sn addition on the corrosion current density of the alloys is two-sided. Compared with the Sn-free alloy, 1.0 wt.% Sn addition makes the corrosion potential (E_{corr}) increase from -1.54 V to -1.50 V, and corrosion current density (I_{corr}) decrease from 1.50×10^{-4} A·cm $^{-2}$ to 2.24×10^{-5} A·cm $^{-2}$. However, as the Sn content increased to 1.5 wt.%, the E_{corr} starts to decrease, while the I_{corr} starts to increase. Furthermore, the Nyquist plots (Figure 4b) show three arcs: a capacitive loop at high frequency, a capacitive loop at medium frequency, and an inductive arc at low frequency. The Bode plots are given in Figure 4c,d, respectively.

Table 4. Parameters of the alloys fitted from potentiodynamic polarization curves.

Alloys	β_a	β_c	I_{corr} (A/cm 2)	E_{corr} (V)
Mg-1Zn	70.67	88.07	1.50×10^{-4}	-1.54
Mg-1Zn-1.0Sn	93.73	119.03	2.24×10^{-5}	-1.50
Mg-1Zn-1.5Sn	97.30	107.64	2.79×10^{-5}	-1.51
Mg-1Zn-2.0Sn	70.10	65.27	3.12×10^{-5}	-1.52

The Mg-1Zn alloy with the smallest capacitive loop at medium frequency indicated the formation of the least protective film. In high and medium frequency regions, the largest capacitive loop radius of the Mg-1Zn-1.0Sn alloy implies the highest impedance value and the lowest corrosion rate, which is consistent with the results of polarization curves. In the equivalent circuit (Figure 4e): R_s is the solution resistance; R_f is the film resistance; CPE is the associated constant phase element in parallel, and it has a capacitance (designated for example as C1,T) and associated phase angle (designated for example as C1,P); R_t is the charge transfer resistance; C is the electrical double-layer capacitor in parallel with the resistive element; and L is the associated inductive element in parallel. These parameters are fitted by ZView and listed in Table 5. It is clear that Mg-1Zn-1.0Sn with the largest arc diameter has the largest value of R_t and R_f , implying the best corrosion resistance. Figure 4f

illustrates the corresponding physical model, of which there is a partly protective film, and it tends to become more protective with increasing immersion time before the film breaks.

Table 5. Parameters of the circuit model fitted from the Nyquist plot.

Samples	Mg-1Zn	Mg-1Zn-1.0Sn	Mg-1Zn-1.5Sn	Mg-1Zn-2.0Sn
R_s (Ωcm^2)	15.4	5.339	12.44	17.89
R_f (Ω/cm^2)	158.4	584	577.3	308.3
C (F/cm^2)	0.0013412	2.3287×10^{-5}	4.6788×10^{-7}	0.00087195
R_f (Ω/cm^2)	494.5	1021	906.3	864.6
CPE1-T (F/cm^2)	5.0867×10^{-5}	0.00026117	0.00026391	3.5368×10^{-5}
CPE1-P (F/cm^2)	0.82682	0.6338	0.6253	0.83465
L (H/cm^2)	427.4	3084	3419	1669

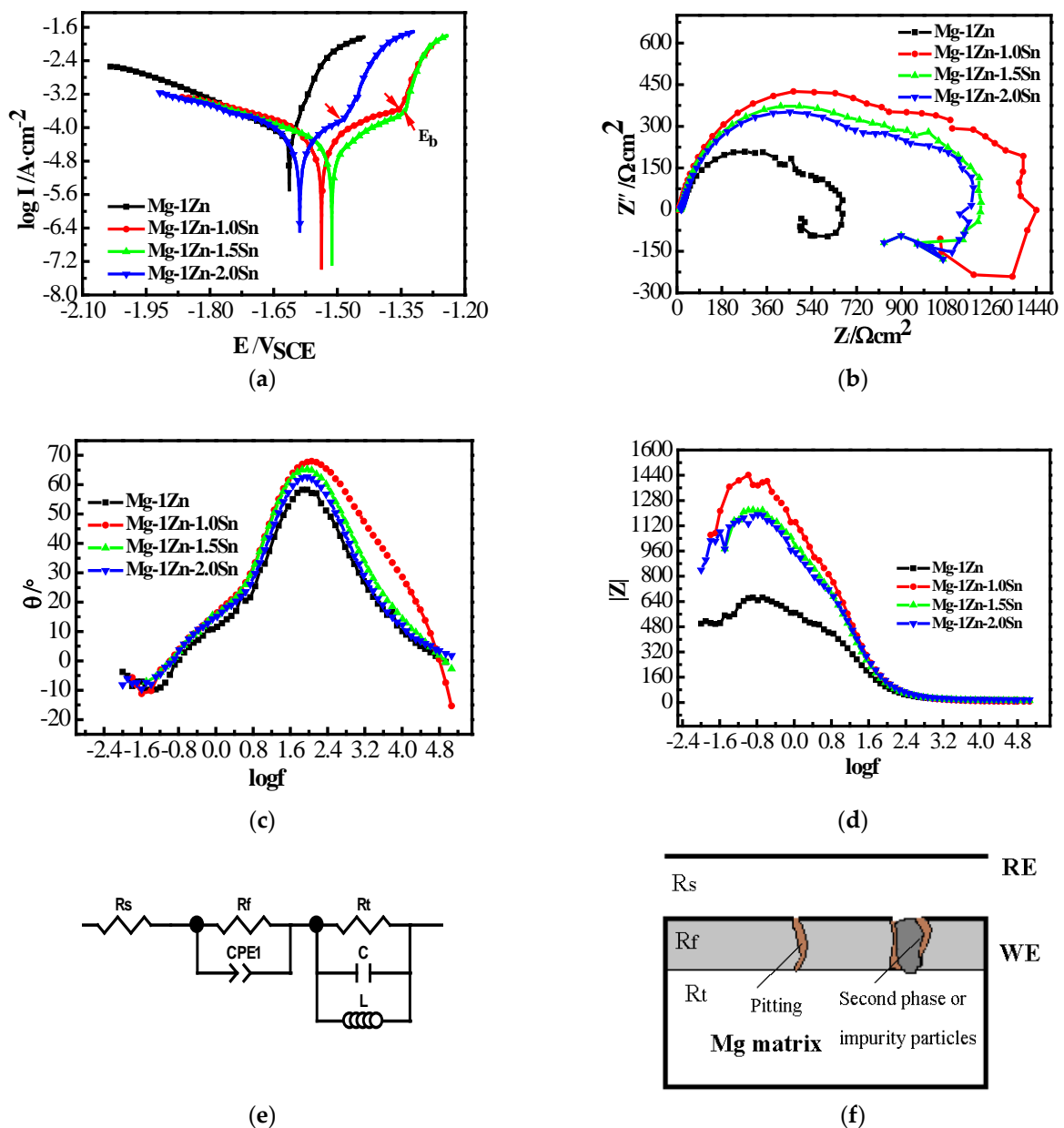


Figure 4. Electrochemical tests results: potentiodynamic polarization curves (a); EIS spectrum-Nyquist plot (b), $|z|$ - $\log f$ plot (c), and θ - $\log f$ plot (d) of the alloys; equivalent circuit model (e) and physical model (f). RE = reference electrode, WE = working electrode.

Figure 5a,b present the hydrogen release and the weight loss rates of the investigated alloys, respectively. All the results show the same trend in the following order: Mg-1Zn > Mg-1Zn-2.0Sn > Mg-1Zn-1.5Sn > Mg-1Zn-1.0Sn. In general, the corrosion rate decreased with the incremental addition of Sn, while it increased as Sn exceeded 1.5. Among the alloys, Mg-1Zn-1.0Sn shows the smallest hydrogen evolution volume of 0.021 mL/cm²/day and the lowest degradation rate of 0.12 mm/y within seven days of immersion. The pH variation during seven days of immersion in Figure 5c indicates that the pH increase for Sn-containing Mg-1Zn alloys is much slower than that for the Mg-1Zn alloy. Since both Mg-1Zn-1.0Sn and Mg-1Zn-1.5Sn alloys exhibit a very low degradation rate, the results of hydrogen evolution volume are compared with some typical biodegradable Mg alloys in the literature, as shown in Figure 5d. Compared with the Mg-1Zn-(0.2, 0.8) Sr alloys [37] and HP Mg, WZ21, and AZ91 alloys [38], the alloys presented in this work possess a prominent advantage of lower in vitro degradation rates.

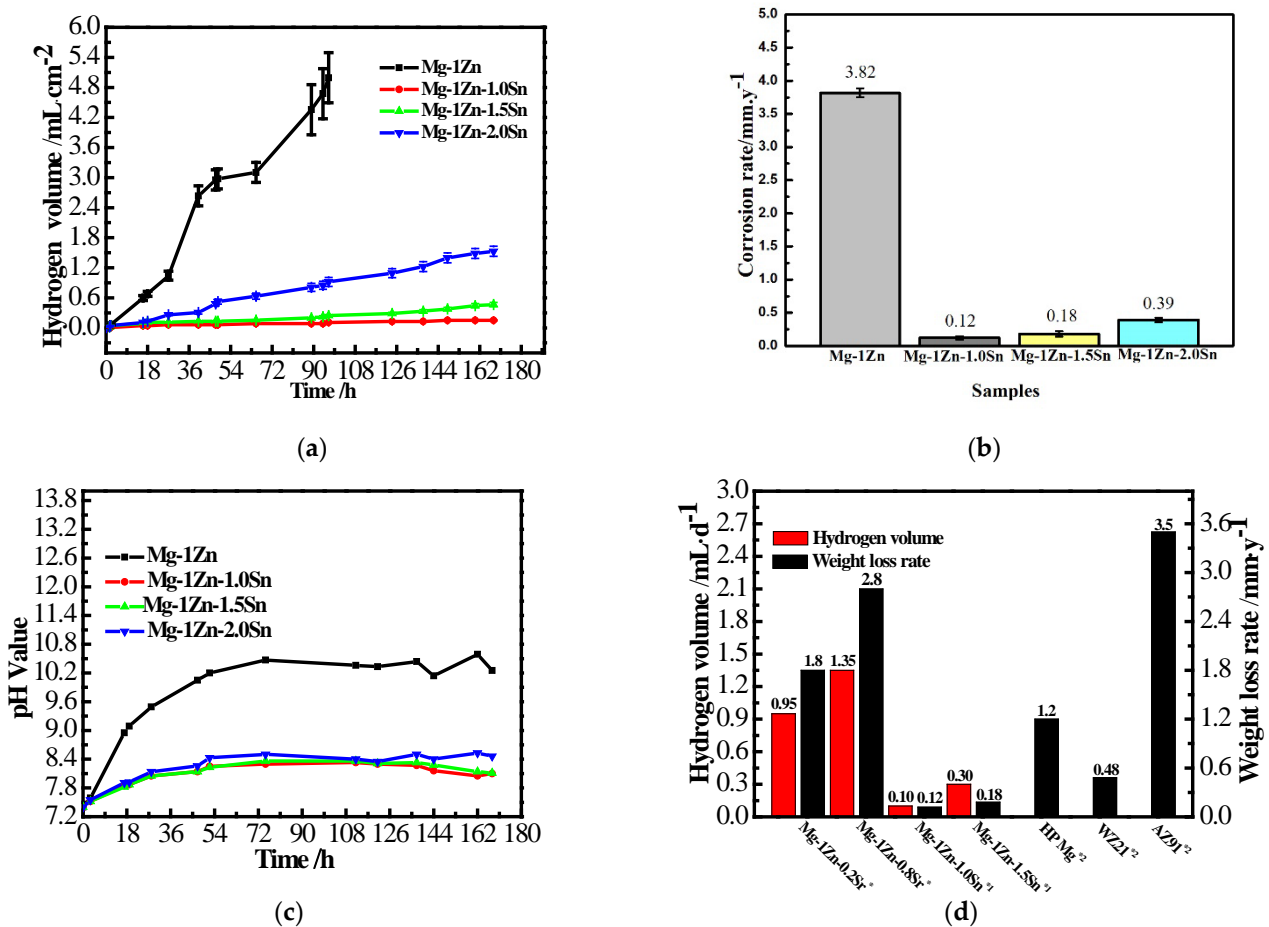


Figure 5. Immersion test results: hydrogen evolution (a), corrosion rate (b) by weight loss, and pH variation (c) of solution for Mg-1Zn-xSn ternary alloys; degradation rate comparison (d) with some typical alloys.

As a reduction in the degradation rate is always associated with the characteristics of the formed corrosion products, samples after seven days immersion were measured by XRD (Figure 6). It can be seen that the products are mainly Mg(OH)₂. Additionally, MgSnO₃ appears in Sn-containing alloys. To clarify the formation process of the corrosion products, the Mg-1Zn-1.0Sn alloy was soaked in PBS for 1h, and then examined by Multi-function X-ray photoelectron spectrometer (XPS) (ESCALAB 250Xi 18000383). It confirmed the presence of magnesium in the form of hydroxide and oxide (Figure 7). Moreover, the existence of SnO₂ demonstrates that Sn participated in the formation of protective film.

Since SnO_2 is difficult to dissolve in aqueous solution and could suppress the corrosion proceeding, SnO_2 can react with dissolved Mg ions to form MgSnO_3 , which can improve the compactness of the surface products, and further played the role of corrosion barrier to resist the corrosive ions.

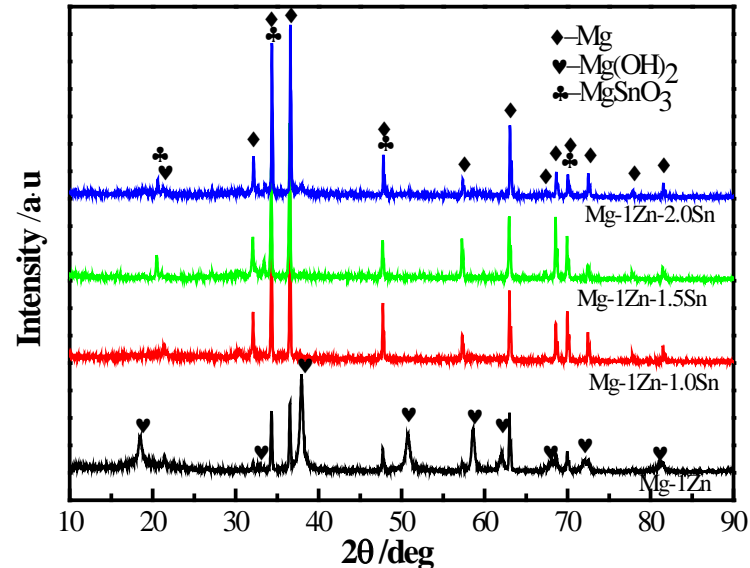


Figure 6. XRD patterns of the corroded alloys with corrosion products.

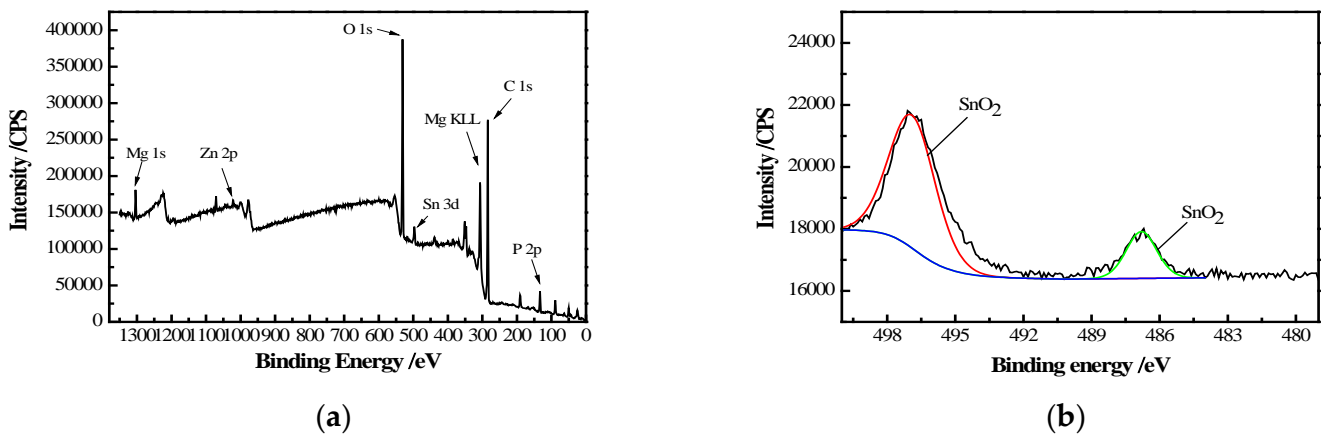


Figure 7. XPS survey spectra (a) and detailed spectra of Sn 3d (b) of corrosion products for Mg-1Zn-1.0Sn after immersion in PBS at 37 °C for 1 h.

As reported, Sn addition can not only increase the compactness of the surface film but also enhance the corrosion resistance of the Mg matrix [39]. Thus, the controlled degradation rate can be attributed to this combined effect. To understand the influence of Sn addition more clearly, the naked appearance of corroded alloys after seven days immersion was examined. Figure 8a–d present the macro-surface appearance of alloys without corrosion products. Serious localized corrosion occurred in Mg-1Zn and Mg-1Zn-2.0Sn alloys. On the contrary, the other two alloys show a relatively even surface with scarcely any traces of corrosion. The corresponding magnified photos shown in the insets revealed the details of the corroded sites. Inside the corroded sites, honeycomb cavities of Mg-1Zn and Mg-1Zn-2.0Sn alloys could provide the channels for the corrosive ions and help the metal dissolution. Conversely, no obvious visible pits can be found on the surface of Mg-1Zn-1.0Sn and Mg-1Zn-1.5Sn alloys, which are characterized by uniform superficial corrosion.

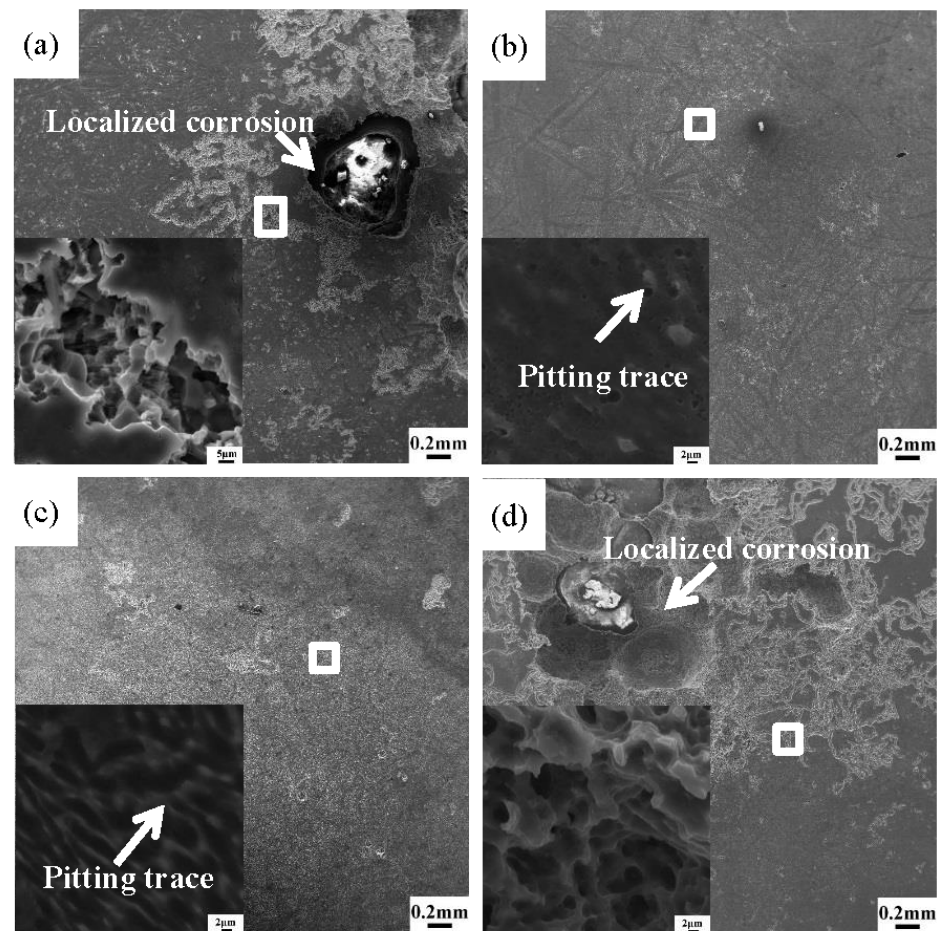
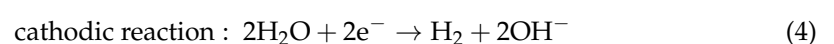
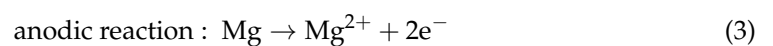


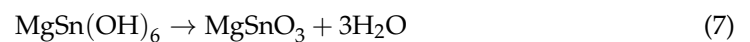
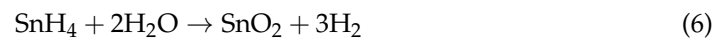
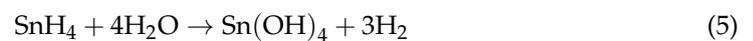
Figure 8. Corroded surface of alloys with corresponding magnified views in the insets, after seven days' soak by SEM: Mg-1Zn (a), Mg-1Zn-1.0Sn (b), Mg-1Zn-1.5Sn (c) and Mg-1Zn-2.0Sn (d).

In the present study, micro-galvanic corrosion influenced by second phases is slight, as most of the Zn and Sn dissolved in the matrix. The dissolved Sn increased the compactness of the Mg substrate, which provided no direct pathway for medium transportation, and made the alloy less prone to pitting pits. In addition, the corrosive ions were prevented from interpenetrating so that pitting corrosion was hindered. Thus, the corrosion pits left on the surface of Mg-1Zn-1.0Sn and Mg-1Zn-1.5Sn are superficial. Moreover, the propagation of corrosion traces is also related to cathode reaction. As one of the limited elements of high hydrogen evolution overvoltage, Sn could inhibit cathode hydrogen evolution [39]. Therefore, the cathode hydrogen evolution of Sn-containing Mg-1Zn alloys was further suppressed compared with the Mg-1Zn alloy. That is to say, the corrosion pits of Sn-containing alloys propagated at a lower velocity than those of the Mg-1Zn alloy. Finally, the pitting corrosion developed into a localized corrosion in Mg-1Zn alloys, but was converted to a uniform corrosion mode by a proper amount of Sn addition. When the Sn content reached 2.0 wt.%, the coarse and increased second phases (Figure 1d) would act as sources of cracks and the initial sites of cathode reaction resulting in the susceptibility to localized corrosion. Up to this state, the detrimental effect overwhelmed the corrosion inhibition effect, and the biodegradation performance deteriorated inversely.

Generally, the corrosion mechanism of magnesium alloy in aqueous solution can be described by the following reactions [10]:



The result of the reactions is the formation of $\text{Mg}(\text{OH})_2$, which will dissolve slightly as the solubility product (K_{sp}) is 1.8×10^{-11} [40]. The existence of chloride ions (Cl^-) in PBS solution will accelerate the dissolution of $\text{Mg}(\text{OH})_2$ by forming soluble MgCl_2 . Thus, Mg^{2+} would be released and the concentration of OH^- increased. The XRD results (Figure 6) show that $\text{Mg}(\text{OH})_2$ and MgSnO_3 are found in the Sn-containing alloys. It is demonstrated that Sn participated in the corrosion product film formation by XPS (Figure 7). According to the Pourbaix E-pH diagram of Sn-H₂O [39], tin hydride (SnH_4) might form first. It was reported that SnH_4 can be formed in the 3.5% NaCl solution with the Mg-xSn alloy [41]. SnH_4 can react with water to form $\text{Sn}(\text{OH})_4$ or SnO_2 (Equations (5) and (6)). In alkaline solution, $\text{Sn}(\text{OH})_4$ would adopt the form of $\text{Sn}(\text{OH})_6^{2-}$ and easily combine with Mg^{2+} to form MgSnO_3 through the reaction (7) [42]. The existence of MgSnO_3 could significantly improve the compactness of the corrosion products on the surface of the Sn-bearing alloys due to the chemical stability of magnesium stannate compounds [43].



It has been proposed that biomaterials with a corrosion rate lower than 0.5 mm/y are promising candidates for biodegradable material to ensure the recovery of bone tissue [44]. The Mg-1Zn-1.0Sn alloy, with a weight loss rate of only 0.12 mm/y, which is far below the critical value, might be potentially outstanding in orthopedic applications in the future.

3.4. Cytocompatibility

The interactions between cells and biomaterials are tested by cells co-culture. Figure 9 shows the cell viability of preosteoblasts (MC3T3-E1) co-cultured in the negative control group, pure Mg (as comparison), and the Mg-1Zn-1.0Sn alloy extraction medium for 72 h, respectively. It is obvious that both samples exhibited higher cell viability than the negative control group, and the cytotoxicity was of grades 0–1 [45], demonstrating that they could be safe and worthwhile for further in vivo investigation. In fact, Mg alloys extractions are always diluted to 10% for cytotoxicity testing [46], and the 10% extraction shows cytotoxicity of grade 0 herein. Figure 9 reveals the cell microfilaments of MC3T3-E1 cells co-cultured with 10% pure Mg, Mg-1Zn-1.0Sn alloy extraction, and the blank control group. The images of cell immunofluorescence were observed by CLSM. The cells co-cultured with 10% extraction exhibit a confluent morphology, and cells are linked to each other with more actin filaments, whereas a monolayer and dispersive morphology with fewer actin filaments is exhibited in the blank control. The quantity of cells in the extractions was larger than in the blank control. All this demonstrates that the Mg-1Zn-1.0Sn alloy presents a good cytocompatibility and cell spreading.

A moderate concentration of Mg^{2+} and a low release of Zn^{2+} could benefit the growth and development of cells [47,48]. The direct cell attachment and proliferation can be assessed by cells adhesion on samples. MC3T3-E1 cells were seeded on pure Mg and Mg-1Zn-1.0Sn alloy, and were examined by SEM (Figure 10) after 24 h culture. Scarcely any cells except a small one designated by a red square can be found in Figure 10a. In Figure 10b, the amplified view of the red square in Figure 10a shows a small, shriveled, and deformed cell marked by a red arrow. It can be attributed to the local alkalization caused by the fast degradation of Mg. On the other hand, several distinct, large cells attach well on the Mg-1Zn-1.0Sn alloy in Figure 10c. One of the cells is squared in red and enlarged in detail in Figure 10d. It grows flat, and has normal forms on the surface, with distinct pseudopod designated by red arrows, which indicates that this alloy has good affinity to cells and is favorable for cells attachment and growth [49–52].

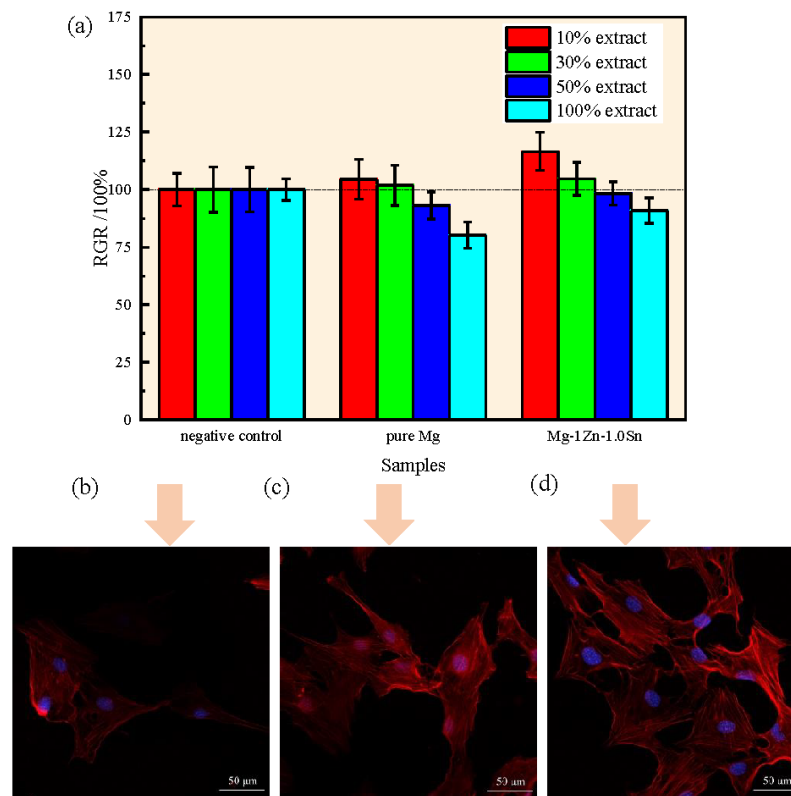


Figure 9. MC3T3-E1 cells viability (a) in solutions containing different concentrations of extract incubated for 72 h by CCK-8 method, and the corresponding cells co-cultured after 24 h incubation with negative control (b), pure Mg (c), and Mg-1Zn-1.0Sn (d) characterized by CLSM.

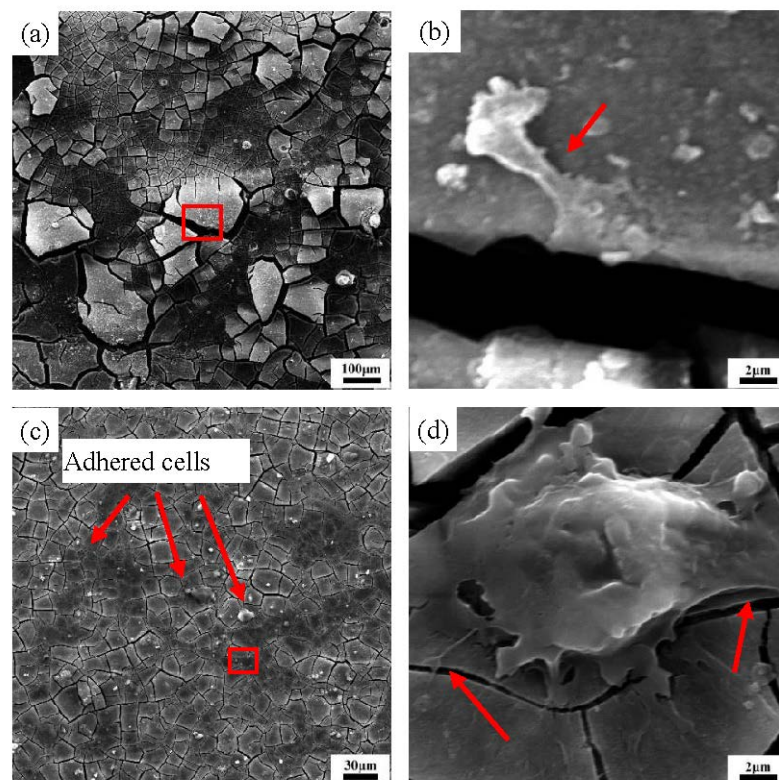


Figure 10. Cells (MC3T3-E1) adhered on the samples: pure Mg (a); magnified view (b) of red square in (a); Mg-1Zn-1.0Sn alloy (c); magnified view (d) of red square in (c).

4. Conclusions

The microstructure, mechanical properties, and in vitro degradation properties of as-extruded Mg-1Zn-based alloys were investigated systematically in the present study. The in vitro degradation tests showed that the Mg-1Zn alloy suffered severe localized corrosion, while alloys with low Sn content presented flat surfaces with little corrosion traces. Although Sn addition in Mg-1Zn alloys decreased the degradation rate, largely by converting the pitting corrosion to a uniform corrosion mode, excessive addition of Sn (above 1.5) conversely deteriorated the degradation performance due to the formation of coarse Mg₂Sn phases. As a new low-alloying magnesium alloy, Mg-1Zn-based alloys display a controllable degradation rate. More specifically, the Mg-1Zn-1.0Sn alloy, with the ultimate tensile strength of 259 MPa, yield strength of 118 MPa, and elongation of 20.2%, exhibited a very low degradation rate of 0.12 mm/y, and a good cytocompatibility to MC3T3-E1 cells, and has a prospective future in orthopedic applications.

Author Contributions: The manuscript was written thanks to the contributions of all the authors. All the authors have given approval to the final version of the manuscript. W.J. and W.Y. guided the research ideas of this work and were responsible for the experimental scheme and the submission of the manuscript. W.J. was in charge of the research and acquisition, analysis and interpretation of data, and manuscript writing. W.Y. offered instructions for writing and revising the manuscript. All authors have read and agreed to the published version of the manuscript.

Funding: This research was funded by the National Natural Science Foundation of China (51704053), the Fundamental and Frontier Research Project of Chongqing, China, grant number (No. cstc2021jcyj-msxmX0830), and the Scientific Research Project for High-level Talents (1956059).

Institutional Review Board Statement: Not applicable.

Informed Consent Statement: Informed consent was obtained from all subjects involved in the study.

Data Availability Statement: Not applicable.

Conflicts of Interest: The authors declare no conflict of interest.

References

1. Agarwal, S.; Curtin, J.; Duffy, B.; Jaiswal, S. Biodegradable magnesium alloys for orthopaedic applications: A review on corrosion, biocompatibility and surface modifications. *Mater. Sci. Eng. C* **2016**, *68*, 948–963. [[CrossRef](#)] [[PubMed](#)]
2. Esmaily, M.; Svensson, J.E.; Fajardo, S.; Birbilis, N.; Frankel, G.S.; Virtanen, S.; Arrabal, R.; Thomas, S.; Johansson, L.G. Fundamentals and advances in magnesium alloy corrosion. *Prog. Mater. Sci.* **2017**, *89*, 92–193. [[CrossRef](#)]
3. Li, X.; Liu, X.; Wu, S.; Yeung, K.; Zheng, Y.; Chu, P.K. Design of magnesium alloys with controllable degradation for biomedical implants: From bulk to surface. *Acta Biomater.* **2016**, *45*, 2–30. [[CrossRef](#)] [[PubMed](#)]
4. Zhang, X.; Li, X.-W.; Li, J.-G.; Sun, X.-D. Preparation and Characterizations of Bioglass Ceramic Cement/Ca-P Coating on Pure Magnesium for Biomedical Applications. *ACS Appl. Mater. Interfaces* **2013**, *6*, 513–525. [[CrossRef](#)]
5. Wu, G.; Zeng, X.; Yuan, G. Growth and corrosion of aluminum PVD-coating on AZ31 magnesium alloy. *Mater. Lett.* **2008**, *62*, 4325–4327. [[CrossRef](#)]
6. Gu, X.; Zhou, W.; Zheng, Y.; Liu, Y.; Li, Y. Degradation and cytotoxicity of lotus-type porous pure magnesium as potential tissue engineering scaffold material. *Mater. Lett.* **2010**, *64*, 1871–1874. [[CrossRef](#)]
7. Bobe, K.; Willbold, E.; Morgenthal, I.; Andersen, O.; Studnitzky, T.; Nellesen, J.; Tillmann, W.; Vogt, C.; Vano, K.; Witte, F. In vitro and in vivo evaluation of biodegradable, open-porous scaffolds made of sintered magnesium W4 short fibres. *Acta Biomater.* **2013**, *9*, 8611–8623. [[CrossRef](#)]
8. Xu, W.; Birbilis, N.; Sha, G.; Wang, Y.; Daniels, J.; Xiao, Y.; Ferry, M. A high-specific-strength and corrosion-resistant magnesium alloy. *Nat. Mater.* **2015**, *14*, 1229–1235. [[CrossRef](#)]
9. Witte, F.; Kaese, V.; Haferkamp, H.; Switzer, E.; Meyer-Lindenberg, A.; Wirth, C.J.; Windhagen, H. In vivo corrosion of four magnesium alloys and the associated bone response. *Biomaterials* **2005**, *26*, 3557–3563. [[CrossRef](#)]
10. Liu, Q.; Ma, Q.-X.; Chen, G.-Q.; Cao, X.; Zhang, S.; Pan, J.-L.; Zhang, G.; Shi, Q.-Y. Enhanced corrosion resistance of AZ91 magnesium alloy through refinement and homogenization of surface microstructure by friction stir processing. *Corros. Sci.* **2018**, *138*, 284–296. [[CrossRef](#)]
11. Song, Y.; Shan, D.; Chen, R.; Zhang, F.; Han, E.-H. Biodegradable behaviors of AZ31 magnesium alloy in simulated body fluid. *Mater. Sci. Eng. C* **2009**, *29*, 1039–1045. [[CrossRef](#)]

12. Hort, N.; Huang, Y.; Fechner, D.; Störmer, M.; Blawert, C.; Witte, F.; Vogt, C.; Drücker, H.; Willumeit, R.; Kainer, K.U.; et al. Magnesium alloys as implant materials—Principles of property design for Mg—RE alloys. *Acta Biomater.* **2010**, *6*, 1714–1725. [[CrossRef](#)]
13. Yang, L.; Hort, N.; Laipple, D.; Höche, D.; Huang, Y.; Kainer, K.U.; Willumeit, R.; Feyerabend, F. Element distribution in the corrosion layer and cytotoxicity of alloy Mg–10Dy during in vitro biodegradation. *Acta Biomater.* **2012**, *9*, 8475–8487. [[CrossRef](#)]
14. Niu, J.; Xiong, M.; Guan, X.; Zhang, J.; Huang, H.; Pei, J.; Yuan, G. The in vivo degradation and bone-implant interface of Mg–Nd–Zn–Zr alloy screws: 18 months post-operation results. *Corros. Sci.* **2016**, *113*, 183–187. [[CrossRef](#)]
15. Kubásek, J.; Vojtěch, D.; Lipov, J.; Ruml, T. Structure, mechanical properties, corrosion behavior and cytotoxicity of biodegradable Mg–X (X=Sn, Ga, In) alloys. *Mater. Sci. Eng. C* **2013**, *33*, 2421–2432. [[CrossRef](#)]
16. Zhang, S.; Zhang, X.; Zhao, C.; Li, J.; Song, Y.; Xie, C.; Tao, H.; Zhang, Y.; He, Y.; Jiang, Y.; et al. Research on an Mg–Zn alloy as a degradable biomaterial. *Acta Biomater.* **2010**, *6*, 626–640. [[CrossRef](#)]
17. Zhang, E.; Yang, L. Microstructure, mechanical properties and bio-corrosion properties of Mg–Zn–Mn–Ca alloy for biomedical application. *Mater. Sci. Eng. A* **2008**, *497*, 111–118. [[CrossRef](#)]
18. Li, H.; Liu, D.; Zhao, Y.; Jin, F.; Chen, M. The Influence of Zn Content on the Corrosion and Wear Performance of Mg–Zn–Ca Alloy in Simulated Body Fluid. *J. Mater. Eng. Perform.* **2016**, *25*, 3890–3895. [[CrossRef](#)]
19. Kubásek, J.; Vojtěch, D. Structural characteristics and corrosion behavior of biodegradable Mg–Zn, Mg–Zn–Gd alloys. *J. Mater. Sci. Mater. Med.* **2013**, *24*, 1615–1626. [[CrossRef](#)]
20. Lu, Y.; Bradshaw, A.; Chiu, Y.; Jones, I. Effects of secondary phase and grain size on the corrosion of biodegradable Mg–Zn–Ca alloys. *Mater. Sci. Eng. C* **2015**, *48*, 480–486. [[CrossRef](#)]
21. Gu, X.; Zheng, Y.; Cheng, Y.; Zhong, S.; Xi, T. In vitro corrosion and biocompatibility of binary magnesium alloys. *Biomaterials* **2009**, *30*, 484–498. [[CrossRef](#)] [[PubMed](#)]
22. Ghayad, I.M.; Maamoun, M.A.; Metwally, W.A.; El-Baradie, Z.M.; Abdel-Azim, A.N. Corrosion Behavior and Surface Modification of Mg–Zn Implant Alloys. *J. Mater. Eng. Perform.* **2016**, *25*, 4171–4180. [[CrossRef](#)]
23. Zhang, E.; He, W.; Du, H.; Yang, K. Microstructure, mechanical properties and corrosion properties of Mg–Zn–Y alloys with low Zn content. *Mater. Sci. Eng. A* **2008**, *488*, 102–111. [[CrossRef](#)]
24. Huan, Z.G.; Leeftang, M.A.; Zhou, J.; Fratila-Apachitei, L.E.; Duszczek, J. In vitro degradation behavior and cytocompatibility of Mg–Zn–Zr alloys. *J. Mater. Sci. Mater. Med.* **2010**, *21*, 2623–2635. [[CrossRef](#)]
25. Song, Y.; Han, E.-H.; Shan, D.; Yim, C.D.; You, B.S. The effect of Zn concentration on the corrosion behavior of Mg–xZn alloys. *Corros. Sci.* **2012**, *65*, 322–330. [[CrossRef](#)]
26. Turen, Y. Effect of Sn addition on microstructure, mechanical and casting properties of AZ91 alloy. *Mater. Des.* **2013**, *49*, 1009–1015. [[CrossRef](#)]
27. Zhao, C.; Pan, F.; Zhao, S.; Pan, H.; Song, K.; Tang, A. Preparation and characterization of as-extruded Mg–Sn alloys for orthopedic applications. *Mater. Des.* **2015**, *70*, 60–67. [[CrossRef](#)]
28. ASTM-G102-89; Standard Practice for Calculation for Corrosion Rates and Related Information from Electrochemical Measurements, Annual Book of ASTM Standards. American Society for Testing and Materials: Philadelphia, PA, USA, 1999.
29. ASTM-G31-72; Standard Practice for Laboratory Immersion Corrosion Testing of Metals, Annual Book of ASTM Standards. American Society for Testing and Materials: Philadelphia, PA, USA, 2004.
30. Wei, S.; Zhu, T.; Hodgson, M.; Gao, W. Effects of Sn addition on the microstructure and mechanical properties of as-cast, rolled and annealed Mg–4Zn alloys. *Mater. Sci. Eng. A* **2013**, *585*, 139–148. [[CrossRef](#)]
31. Xiao, W.; Jia, S.; Wang, L.; Wu, Y.; Wang, L. Effects of Sn content on the microstructure and mechanical properties of Mg–7Zn–5Al based alloys. *Mater. Sci. Eng. A* **2010**, *527*, 7002–7007. [[CrossRef](#)]
32. Wang, B.; Pan, F.; Chen, X.; Guo, W.; Mao, J. Microstructure and mechanical properties of as-extruded and as-aged Mg–Zn–Al–Sn alloys. *Mater. Sci. Eng. A* **2016**, *656*, 165–173. [[CrossRef](#)]
33. Liu, C.; Chen, H.; Nie, J.-F. Interphase boundary segregation of Zn in Mg–Sn–Zn alloys. *Scr. Mater.* **2016**, *123*, 5–8. [[CrossRef](#)]
34. Hong, D.; Saha, P.; Chou, D.-T.; Lee, B.; Collins, B.E.; Tan, Z.; Dong, Z.; Kumta, P.N. In vitro degradation and cytotoxicity response of Mg–4% Zn–0.5% Zr (ZK40) alloy as a potential biodegradable material. *Acta Biomater.* **2013**, *9*, 8534–8547. [[CrossRef](#)] [[PubMed](#)]
35. Zhang, X.; Yuan, G.; Mao, L.; Niu, J.; Ding, W. Biocorrosion properties of as-extruded Mg–Nd–Zn–Zr alloy compared with commercial AZ31 and WE43 alloys. *Mater. Lett.* **2012**, *66*, 209–211. [[CrossRef](#)]
36. Song, G.-L. Effect of tin modification on corrosion of AM70 magnesium alloy. *Corros. Sci.* **2009**, *51*, 2063–2070. [[CrossRef](#)]
37. Li, H.; Peng, Q.; Li, X.; Li, K.; Han, Z.; Fang, D. Microstructures, mechanical and cytocompatibility of degradable Mg–Zn based orthopedic biomaterials. *Mater. Des.* **2014**, *58*, 43–51. [[CrossRef](#)]
38. Abidin, N.I.Z.; Rolfe, B.; Owen, H.; Malisano, J.; Martin, D.; Hofstetter, J.; Uggowitzer, P.; Atrens, A. The in vivo and in vitro corrosion of high-purity magnesium and magnesium alloys WZ21 and AZ91. *Corros. Sci.* **2013**, *75*, 354–366. [[CrossRef](#)]
39. Liu, X.; Shan, D.; Song, Y.; Chen, R.; Han, E. Influences of the quantity of Mg₂Sn phase on the corrosion behavior of Mg–7Sn magnesium alloy. *Electrochim. Acta* **2011**, *56*, 2582–2590. [[CrossRef](#)]
40. Cao, C.N. *Principles of Corrosion Electrochemistry*; Chemical Industry Press: Beijing, China, 2004.
41. Wang, J.; Li, Y.; Huang, S.; Zhou, X. Study of the corrosion behavior and the corrosion films formed on the surfaces of Mg–xSn alloys in 3.5 wt.% NaCl solution. *Appl. Surf. Sci.* **2014**, *317*, 1143–1150. [[CrossRef](#)]
42. Moon, S.; Nam, Y. Anodic oxidation of Mg–Sn alloys in alkaline solutions. *Corros. Sci.* **2012**, *65*, 494–501. [[CrossRef](#)]

43. Du, W.; Liu, K.; Ma, K.; Wang, Z.; Li, S. Effects of trace Ca/Sn addition on corrosion behaviors of biodegradable Mg–4Zn–0.2Mn alloy. *J. Magnes. Alloy.* **2018**, *6*, 1–14. [[CrossRef](#)]
44. Erinc, M.; Sillekens, H.; Mannens, R.; Werkhoven, R.J. Applicability of existing magnesium alloys as biomedical implant materials. *Magnes. Technol.* **2009**, 209–214.
45. Cheng, J.; Liu, B.; Wu, Y.; Zheng, Y. Comparative in vitro Study on Pure Metals (Fe, Mn, Mg, Zn and W) as Biodegradable Metals. *J. Mater. Sci. Technol.* **2013**, *29*, 619–627. [[CrossRef](#)]
46. He, R.; Liu, R.; Chen, Q.; Zhang, H.; Wang, J.; Guo, S. In vitro degradation behavior and cytocompatibility of Mg–6Zn–Mn alloy. *Mater. Lett.* **2018**, *228*, 77–80. [[CrossRef](#)]
47. Zhang, S.; Zheng, Y.; Zhang, L.; Bi, Y.; Li, J.; Liu, J.; Yu, Y.; Guo, H.; Li, Y. In vitro and in vivo corrosion and histocompatibility of pure Mg and a Mg–6Zn alloy as urinary implants in rat model. *Mater. Sci. Eng. C* **2016**, *68*, 414–422. [[CrossRef](#)]
48. Li, Y.; Li, H.; Zhang, J.; Zhao, W.; Shen, J.; Jiang, D. In vitro evaluation of an yttria-stabilized zirconia reinforced nano-hydroxyapatite/polyamide 66 ternary biomaterial: Biomechanics, biocompatibility and bioactivity. *RSC Adv.* **2016**, *6*, 114086–114095. [[CrossRef](#)]
49. Gurel, S.; Nazarahari, A.; Canadinc, D.; Cabuk, H.; Bal, B. Assessment of biocompatibility of novel TiTaHf-based high entropy alloys for utility in orthopedic implants. *Mater. Chem. Phys.* **2021**, *266*, 124573. [[CrossRef](#)]
50. Jiang, W.; Yu, W. Corrosion Behavior and Osteogenic Activity of a Biodegradable Orthopedic Implant Mg–Si Alloy with a Gradient Structure. *Metals* **2021**, *11*, 781. [[CrossRef](#)]
51. Tan, J.K.; Balan, P.; Birbilis, N. Advances in LDH coatings on Mg alloys for biomedical applications: A corrosion perspective. *Appl. Clay Sci.* **2020**, *202*, 105948. [[CrossRef](#)]
52. Rahman, M.; Li, Y.; Wen, C. HA coating on Mg alloys for biomedical applications: A review. *J. Magnes. Alloy.* **2020**, *8*, 929–943. [[CrossRef](#)]